Insights into Ni and (Ce)SBA-15-CTA interaction and syngas formation rate

Luming Li[a,b,c], Dapeng Liu[b], Zhanglong Guo[b,c], Shibo Xi[b], Wei Chu[c,*] Yan Liu[b,*]

[a] Institute for Advanced Study, Chengdu University, Chengdu 610106, China;

[b] Institute of Chemical and Engineering Sciences, A*STAR, 627833, Singapore;

[c] Department of Chemical Engineering, Sichuan University, Chengdu 610065, China.

* **Corresponding authors:** E-mail: liu_yan@ices.a-star.edu.sg (Y. Liu);

chuwei1965@scu.edu.cn (W. Chu).

Abstract: Our SBA-15-CTA mesoporous materials developed in citric acid (CTA), instead of traditional HCl intermediate, was used to support CeO_2 doped nickel catalysts in methane dry reforming reaction. Results revealed that SBA-15-CTA had a high capacity for hosting CeO_2 (up to 30 wt.%), which had strong interaction with Ni species, leading to a high reduction temperature of NiO at 442 ºC. XANES analysis verified that Ni species were much more stable over Ce doped SBA-15-CTA than un-doped ones, which helped the Ni species maintain their metallic state. As demonstrated through TPSR analysis, CH_4 and CO_2 was converted to syngas at a high rate at a low initiation temperature over Ce doped Ni/SBA-15-CTA catalysts. Despite both catalysts having similar performance, Ni/30CeO_2-SBA-15-CTA yielded a much lower coke deposition rate (4.9% vs 22.4% on Ni/10CeO_2-SBA-15-CTA). A desirable endurance to metal sintering and carbon elimination rate was achieved over 5Ni/15CeO_2-SBA-15-CTA catalyst, owing to the high concentration of oxygen vacancy coupled with the high amount of Ce^{3+}.

Keywords: (Ce)SBA-15-CTA; Ni; Dry reforming; Syngas; Oxygen vacancy

1. Introduction

The dry reforming of methane (DRM) process has aroused particular interest, as it can convert two greenhouse gases (CH_4 and CO_2) into syngas (CO and H_2), for the production of sulfur-free liquid fuels and oxygenated chemicals [1-3]. The key issues to be addressed are to design the durable and efficient DRM catalysts. Among the supported noble metal (e.g. Ru, Rh, Pt and Pd) and non-noble metal (e.g. Ni and Co) catalysts [4,5], Ni-based catalysts have attracted more and more attentions due to their low cost, abundant sources, and excellent capability for C-H bond rupture [6].

$$CH_4 + CO_2 \rightleftharpoons 2H_2 + 2CO \ \triangle H_{298}^{\theta} = 247\ KJ/mol \qquad (1)$$

$$2CO \rightleftharpoons C + CO_2 \ \triangle H_{298}^{\theta} = -172\ KJ/mol \qquad (2)$$

$$CH_4 \rightarrow C + 2H_2 \ \triangle H_{298}^{\theta} = 75\ KJ/mol \qquad (3)$$

However, due to the high endothermic property (Eq. 1), the DRM reaction usually operates at high reaction temperature, leading to the sintering of active Ni species. On the other hand, carbon deposition reluctantly happens from the side reactions (Eq. 2 and 3), which would detach Ni nanoparticles from the support and cover Ni surface. Therefore, Ni sintering and carbon deposition are the two major manipulators for catalysts deactivation for DRM reaction over Ni-based catalysts [7-9].

Considerable studies were reported on the effects of support and additives for improving Ni-based catalysts' activity and stability [10]. Various materials such as Al_2O_3, CeO_2, ZrO_2, zeolite, mixed oxides and silica were employed as catalyst supports in DRM [10-12]. Recently, mesoporous silica such as SBA-15, SBA-16, KIT-6 and MCM-41 have attracted increasing attentions due to their high surface areas, long range

ordered mesoporous channels and tunable pore dimension priorities, which would facilitate the well dispersed and confined Ni species, for inhibiting their agglomeration [12,13]. Zhang et al. reported that nickel species were highly dispersed on the SBA-15 compared to that of KIT-6 and MCM-41 carriers and presented an excellent resistance to the carbon deposition [14]. Liu et al found that nano-sized nickel particles with narrow distribution anchored on SBA-15 gave higher activities than Ru catalysts for ammonia decomposition [15]. However, the ordered mesostructured of silica materials still encountered the insufficiency for hindering the sintering of Ni species due to the movability of Ni particles at the elevated temperatures, rising from the inherently weak interaction between Ni and supports [16].

In general, promoters such as ZrO_2, La_2O_3, CaO and CeO_2 were capable of enhancing the dispersion of Ni species and controlling their grain size owing to the strong metal-support interaction. CeO_2, possessing unique physicochemical properties including redox ($Ce^{4+} \leftrightarrow Ce^{3+}$) ability, high oxygen storage capability and thermal resistance, can not only strengthen the metal-support interaction to prevent the sintering of Ni, but also activate carbon dioxide into mobile oxygen and accelerate coke removal [17-19]. Recently, Mehran et al reported that Ni (10 wt.%) supported on CeO_2 (7 wt.%) doped MgO provided the high catalytic performance and anti-coke capacity due to the improved Ni dispersion [11]. Alavi et al studied the effect of nickel and cerium loadings on DRM activity on $ZnAl_2O_4$ support. Results indicated that the optimized catalytic performance was obtained over the catalyst with 5 wt.% of cerium [20]. Moreover, the promotion effect of CeO_2 (loadings varied between 1-5 wt.%) was also observed in Ni-

CeO_2-MgO-Al_2O_3 catalytic system. The cerium loading of 3 wt.% presented the highest resistance to carbon deposition in DRM process [21]. Damyanova et al reported that the average Ni particles size of 4.7-6.3 nm gave the best performance and anti-coke capacity over CeO_2 (6 wt.%) promoted Ni/Al_2O_3 catalyst prepared using incipient wetness-impregnation method [22]. Gong et al presented that ceria-doped Ni/SBA-15 catalyst gave an enhanced stability in the ethanol steam reforming with the Ce/Ni atomic ratio of 1 [16]. In another interesting work, it was found that the incorporation of CeO_2 (14.7 wt.%) could effectively prohibit the agglomeration of nickel (5 wt.%) due to the strong interaction between Ni and ceria in the cage-like pores of SBA-16 [23].

An optimal ceria loading should be taken into consideration in view of the enhanced Ni-CeO_2 interaction and resistance to carbon deposition. Recently, we developed the mesoporous silica (SBA-15-CTA) under moderate polycarboxylic acid medium without introducing inorganic salts and mineral acids, which exhibits the typical 2D hexagonal meso-structure [24]. Herein, we further explored the strong interaction between Ni active species and the SBA-15-CTA hosted CeO_2 at a wide range from 2 to 50 wt.%. Results revealed that SBA-15-CTA had a high capacity for hosting CeO_2 (up to 30 wt.%). Even though having the similar performance to that of Ni/10CeO_2-SBA-15-CTA, Ni/30CeO_2-SBA-15-CTA yielded a much lower coke deposition rate (4.9% vs 22.4%). CH_4 and CO_2 was converted to syngas at a high rate at a low initiation temperature over Ce doped Ni/SBA-15-CTA catalysts. Moreover, the further optimized content (15 wt.%) of CeO_2 depicted a better anti-sintering property

and led to a long catalytic life (170 h) with improved catalytic performance.

2. Experimental

2.1 Materials

Citric acid anhydrous, tetraethyl orthosilicate (≥98%), P123 (Molecular weight: 5800 g mol^{-1}), cerium nitrate hexahydrate, nickel nitrate hexahydrate and ethanol were purchased from Sigma Aldrich. Reagents were used as received.

2.2 Catalysts preparation

xCeO_2-SBA-15-CTA carriers were prepared using the incipient wetness-impregnation method, while mesoporous SBA-15-CTA with S_{BET} = 846.4 m^2/g was synthesized using our reported method under moderate polycarboxylic acid medium (see ref. [24]). A typical procedure was as following: 2g SBA-15-CTA powder were added into an aqueous solution of $Ce(NO_3)_2$ (CeO_2 content at 2-50 wt.%). The slurry was magnetically stirred at agitation rate of 400 rpm for more than 2 h at room temperature. Subsequently, the slurry was transferred to a rotary evaporator (BUCHI Rotavapor R-300), where the pressure of vacuum was fixed at 100 mbar with the rotation speed at 100 rpm, and the temperature of water bath at 55 ºC. After drying at 110 ºC overnight in an oven, the obtained yellow powders were calcined at 450 ºC for 4 h (@ 2 ºC/min) to prepare the CeO_2 doped SBA-15-CTA carriers.

Ni was uploaded to the above CeO_2 doped SBA-15-CTA carriers using the similar procedure, except that the calcination was carried out at 750 ºC (@ 2 ºC/min) for 2 h. Specifically, $Ni(NO_3)_2$ was used as the precursor for achieving 5 wt.% of Ni loadings.

2.3 Catalysts characterization

X-ray diffraction (XRD, 2θ = 5-80º) and low-angle XRD (2θ = 0-6º) were performed on a Bruker D8 Advance X-ray diffractometer using Cu $K\alpha_1$ irradiation. A Micromeritics ASAP 2420 automatic analyzer was engaged to study the N_2 adsorption-desorption properties at -196 ºC for achieving the specific surface area (BET analysis), total pore volume (@ a relative pressure of 0.99). Pretreatments were performed at 200 ºC overnight to remove moisture and other volatile impurities. The contents of various elements were analyzed using an X-ray fluorescence spectrometer (XRF, Bruker, S4 Explorer). Transmission electron microscopy (TEM, FEI Tecnai G2 F20) analysis was done to investigate the microstructure and nickel particle sizes. The X-ray photoelectron spectroscopy (XPS) was measured using an ESCALAB 250 equipped with an Al Kα X-ray (1486.6 eV). The binding energy values were calibrated using the C1s signal (284.6 eV) as internal standard. Ni K-edge X-ray absorption near edge structure (XANES) experiments were performed using XAFCA beamline in the transmission mode at the Singapore Synchrotron Light Source, and Ni K-edge spectra of pre-reduced catalysts were calibrated with respect to the spectrum of a Ni foil and NiO references. The catalysts were pre-reduced at 700 ºC for 1 h under 10 vol.% H_2/He, then cooled down to room temperature under Helium gas.

H_2-TPR (hydrogen-temperature programmed reduction) was carried out in AutoChem II 2920 (Thermo Scientific). Catalysts (30 mg) were pretreated in Ar (30 mL/min) for 1 h at 300 ºC, then cooled down to 50 ºC. H_2-TPR was performed in the

mixture gas of 5 vol% H_2 in Ar (30 mL/min) at 50 - 900 ºC (@ 10 ºC/min), monitoring with a thermal conductivity detector. Thermogravimetric analysis was conducted using a TGA Q500 instrument to assess the coking behaviors on spent catalysts.

2.4 Catalytic activity testing

Dry reforming of methane (DRM) reaction was studied in a fixed-bed quartz reactor (ID: 7 mm) at ambient pressure. Typically, catalysts (150 mg, 45-60 mesh) were uploaded in the central of reactor tube with the support of quartz wool. The catalysts were pre-reduced in 10 vol.% H_2/He (50 mL/min) at 700 ºC (@ 5 ºC/min) for 1 h. Then, the reaction gas (CO_2/CH_4/Ar/N_2 = 3:3:3:1) was introduced to the catalysts bed at a total flow rate of 50 mL/min (GHSV of 20,000 $mL \cdot g_{cat}^{-1} \cdot h^{-1}$). The products were analyzed using online Gas Chromatograph (Agilent GC-6890) equipped with a TCD detector (a Carbon-Plot coupled with a HP-Plot capillary column).

Temperature-programmed surface reaction - mass spectrometry (TPSR-MS) was engaged to investigate the catalytic performance as a function of reaction temperatures. 150 mg catalyst was pre-reduced using the same procedure, then cooled down to 300 ºC (@ 5 ºC/min) in a flow of Helium gas at 45 mL/min. The TPSR-MS analysis was performed under the reaction mixture gas (CO_2/CH_4/Ar = 6:4:15) at 50 mL/min from 300 ºC to 850 ºC (@ 10 ºC/min). The changes of CH_4, CO_2, H_2 and CO components were tracked using mass spectrometer (Hiden MS).

3. Results and discussion

3.1 Catalytic activity of Ni based catalysts in DRM reaction

Fig.1A presented the catalytic activity of 5Ni/xCeO_2-SBA-15-CTA catalysts with different contents of CeO_2. On un-doped 5Ni/SBA-15-CTA catalyst, CH_4 conversion, CO_2 conversion, H_2/CO molar ratio and H_2 selectivity were at 50.2%, 58.7%, 76.8% and 80.5%, respectively. Notably, the corresponding activity values were increased to 72.7%, 77.2%, 89.4% and 92.5% over 5Ni/10CeO_2-SBA-15-CTA catalysts, indicating the great improvement from CeO_2 dopant up to 10 wt.%. While the content of CeO_2 was further increased, the activities didn't change much. CH_4 conversion, CO_2 conversion, H_2/CO molar ratio and H_2 selectivity for 5Ni/30CeO_2-SBA-15-CTA catalyst were 72.2%, 76.9%, 88.9% and 93.3%, being quite similar to those of 5Ni/10CeO_2-SBA-15-CTA catalyst. Results indicate that there exists a wide range of CeO_2 doped contents over SBA-15-CTA supported Ni-based catalysts in view of the improved catalytic activity. On the other hand, it is worth to note that CO_2 conversion was obviously higher than that of CH_4 conversion over all the catalysts. It was mainly attributed to the reversed water gas shift (RWGS) side reaction (Eq (4)), co-existing with DRM [25,26].

$$CO_2 + H_2 \rightleftharpoons CO + H_2O \qquad (4)$$

TGA analysis is an effective technique to assess the anti-coke capacity of the catalysts. As displayed in Fig. 1B, the weight loss on spent 5Ni/xCeO_2-SBA-15-CTA catalysts increased while the content of cerium oxide was up to 5 wt.%, which might be related to the enhanced catalytic performance. Over 5Ni/5CeO_2-SBA-15-CTA spent

catalyst, about 25.5% weight loss was detected. The weight loss was gradually decreased with further increasing CeO_2 contents. Given the very similar catalytic performance on 5Ni/xCeO_2-SBA-15-CTA (x = 10, 15, 30 wt.%) catalysts (Fig. 1A), the weight loss was significantly decreased from 22.4%, to 9.2%, and 4.9%, respectively, which should be contributed to the coke resistance capacity of CeO_2. Higher content of CeO_2 dopants, greater capability for in situ coke removal during DRM reaction.

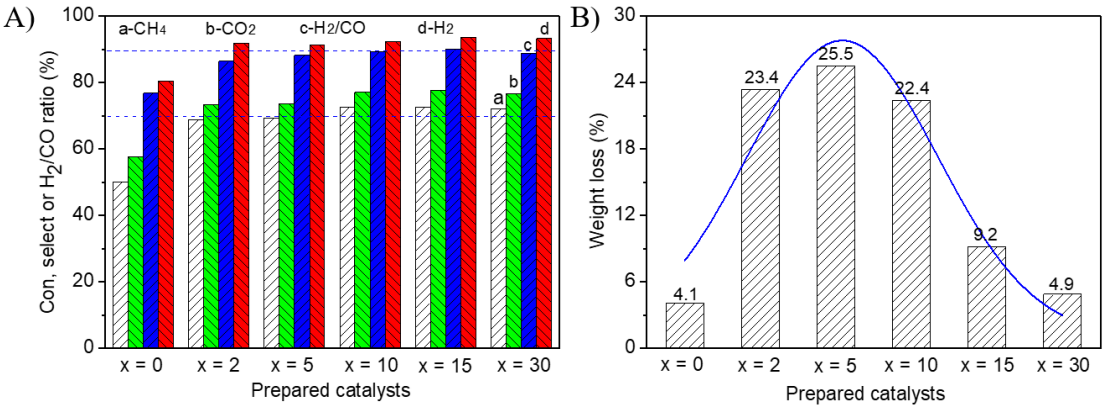

Fig. 1 (A) The catalytic performance on 5Ni/xCeO_2-SBA-15-CTA (a, b, c and d referring to CH_4 and CO_2 conversion, H_2/CO molar ratio and H_2 selectivity, respectively) (B) The weight loss profiles of spent 5Ni/xCeO_2-SBA-15-CTA catalysts (T: 700 ºC; GHSV = 20000 $mL \cdot g_{cat}^{-1} \cdot h^{-1}$; t: 12 h).

Considering the excellent catalytic performance and high anti-coke capacity over 5Ni/10CeO_2-SBA-15-CTA and 5Ni/15CeO_2-SBA-15-CTA catalysts, the long-term stability experiments ware performed, as depicted in Fig. 2A, 2B, 2C. Apparently, both catalysts showed a very good activity and stability, especially for 5Ni/15CeO_2-SBA-15-CTA catalysts. Their initial activities were quite similar during the first 30 h reaction time. However, subsequently, an apparent gap was found and getting more significant

along with the reaction time. Based on the slopes of CO_2 and CH_4 conversions calculated from the stability test, the deactivation rate of 5Ni/10CeO_2-SBA-15-CTA was almost doubled of that for 5Ni/15CeO_2-SBA-15-CTA catalysts, indicating a better anti-coke capacity of 5Ni/15CeO_2-SBA-15-CTA. As shown in Fig. 2D, the coke deposition was only 13.5% over 170 h reaction on the spent 5Ni/15CeO_2-SBA-15-CTA catalyst, being obviously lower than that of the spent 5Ni/10CeO_2-SBA-15-CTA catalysts (25.4% for 96 h reaction). Results strongly demonstrated the remarkable capability of CeO_2 on in situ removal of coke species from the catalysts, being consistent to the results indicated in Fig. 1B.

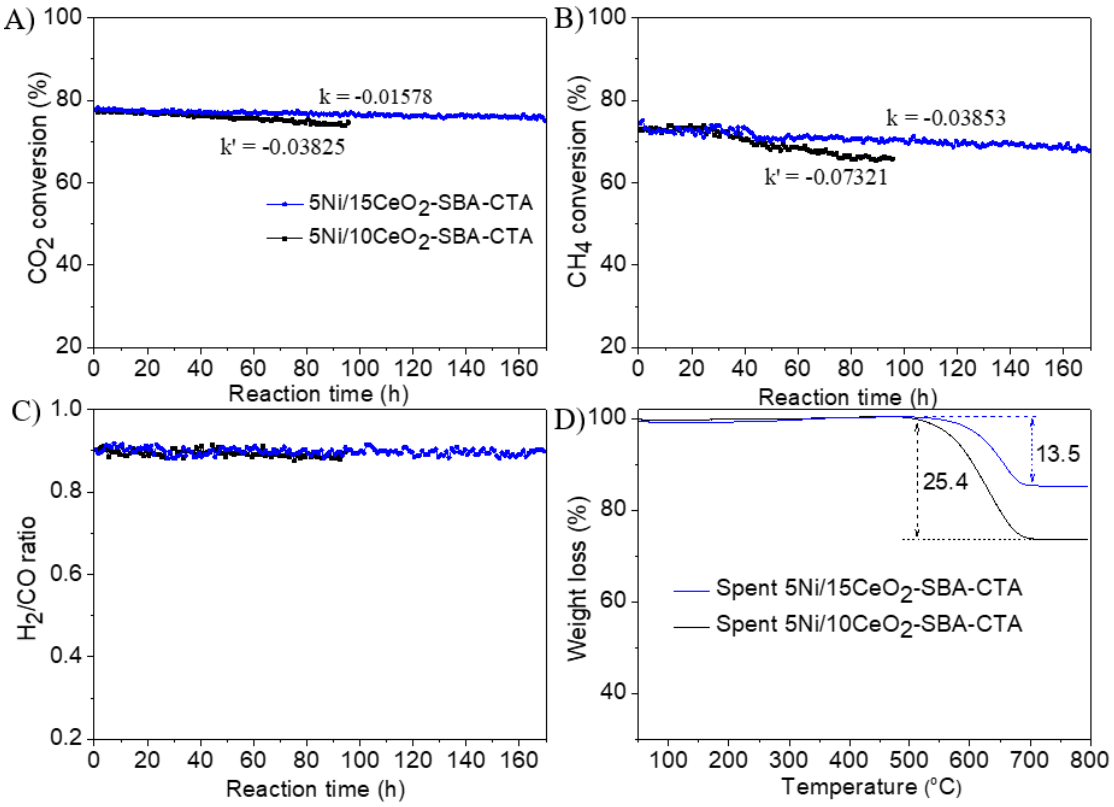

Fig. 2 The stability test over the 5Ni/10CeO_2-SBA-15-CTA and 5Ni/15CeO_2-SBA-15-CTA catalysts. (A) CO_2 conversion (%), (B) CH_4 conversion (%), (C) H_2/CO molar ratio and (D) Weight loss curves of the spent catalysts (700 °C, GHSV=20000 mL·g_{cat}^{-1}·h^{-1}).

.

While co-relating the TGA analysis results in Fig. 2D and Fig. 1B, it was found that the majority of coke deposition was formed at the initial stage of the reaction. Over 12 h reaction time, the coke deposition on 5Ni/10CeO_2-SBA-15-CTA and 5Ni/15CeO_2-SBA-15-CTA catalysts were 22.4% and 9.2%. Further extending reaction time didn't lead to a significant carbon deposition. Only 3% coke deposition was accuminated on 5Ni/10CeO_2-SBA-15-CTA for the next 84 h reaction, while 4.3% coke deposition was generated over 5Ni/15CeO_2-SBA-15-CTA catalysts for the extending 158 h reaction. It was indicated that the dynamic balance between carbon formation and coke removal on catalyst surface could be subsequently reached. The observations implied that the CeO_2 dopants not only improved the catalytic activity but also greatly enhanced the anti-coking capability for SBA-15-CTA supported Ni based catalysts.

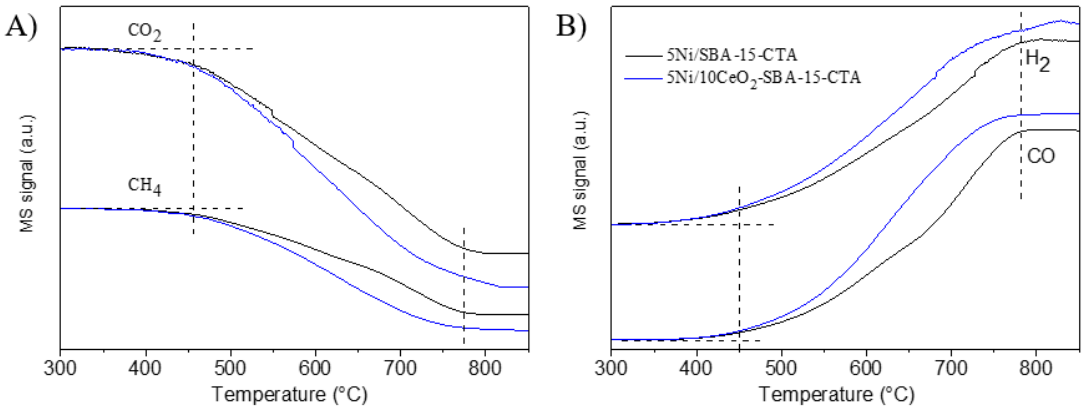

Fig. 3 The catalytic activity of 10 wt.% CeO_2 doped and bare 5Ni/SBA-15-CTA catalysts as a function of reaction temperature (note: the MS signals represent the content of the detected species).

Fig 3 depicted the catalytic performance dependence on reaction temperature using

Temperature Programmed Surface Reaction (TPSR-MS) technique. From the MS analysis, it was found that there was a lower initiation temperature at a higher reaction rate over 10 wt.% CeO_2 doped 5Ni/SBA-15-CTA than the un-doped 5Ni/SBA-15-CTA catalysts in the DRM reaction. Results suggested that CeO_2 doped 5Ni/SBA-15-CTA catalyst had stronger capabilities for activating CO_2 and CH_4 than that of the un-doped 5Ni/SBA-15-CTA catalyst.

3.2 Characterization of CeO_2 doped, un-doped SBA-15-CTA and supported Ni catalysts

3.2.1 Textural properties of the catalysts

It was well accepted that the catalytic performance depends on catalysts' physicochemical properties such as microstructure, various element components and their valence states, particle sizes and redox capability [27,28]. As shown in Fig. 4A, the N_2 adsorption-desorption isotherms of the 5NiO/xCeO_2-SBA-15-CTA catalysts with x value ranges from 0-30 wt.% displayed a type of IV isotherm with H1-type hysteresis loop, indicating the typical characteristic of mesoporous materials based on the IUPAC classification [29]. The pore size distribution for all the catalysts corresponded well with the hysteresis loops shape (Fig. 4B), implying that the mesoporous structure was well preserved after the introduction of Ni and CeO_2 onto SBA-15-CTA matrix [29]. Along with the increase of CeO_2 contents, the specific surface area (S_{BET}) was dropped as expected as listed in Table 1. For example, the S_{BET}

value was 619.8 m^2/g for 5NiO/2CeO_2-SBA-15-CTA with 2 wt.% content of CeO_2, while the surface area was sharply decreased to 377.4 m^2/g for the 5NiO/30CeO_2-SBA-15-CTA with 30 wt.% of CeO_2. It was inferred that the addition of NiO and CeO_2 would block certain SBA-15-CTA pore channels, which became worse at the high contents of CeO_2. It is noted that the specific surface area and total pore volume were relatively higher than those of Ni-CeO_2 catalysts supported on SBA-15-HCl (Table 1), prepared in traditional HCl medium.

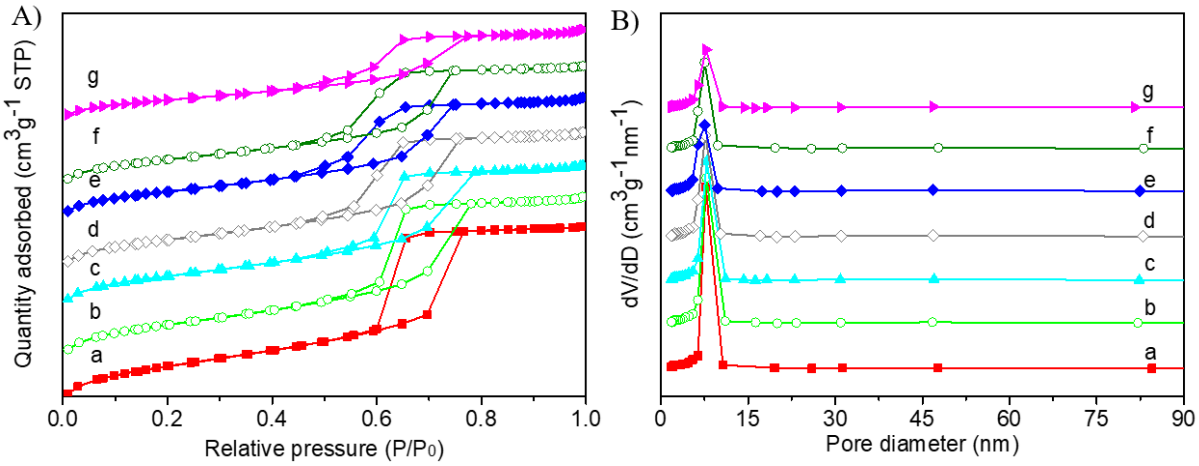

Fig. 4 N_2 adsorption-desorption isotherms (A) and pore size distributions (B) for the for the 5NiO/SBA-15-CTA and the CeO_2 doped 5NiO/SBA-15-CTA catalysts (a) 5NiO/SBA-15-CTA, (b) 5NiO/2CeO_2-SBA-15-CTA, (c) 5NiO/5CeO_2-SBA-15-CTA, (d) 5NiO/10CeO_2-SBA-15-CTA, (e) 5NiO/15CeO_2-SBA-15-CTA, (f) 5NiO/20CeO_2-SBA-15-CTA, (g) 5NiO/30CeO_2-SBA-15-CTA.

Table 1. Textural characteristics of the ceria containing mesoporous silica materials.

NO.	Samples	Content (wt.%)	Crystal size (nm)	Textural properties				
				S_{BET}	V_P	D_p	a_0	w
		Ni/CeO_2[a]	NiO/CeO_2[b]	(m^2/g)	(cm^3/g)	(nm)	(nm)[c]	(nm)[d]
1	5NiO/SBA-15-HCl	4.6/-	12.7/n.a.	571.9	0.78	6.04	10.81	4.77
2	5NiO/SBA-15-CTA	5.0/-	11.8/n.a.	665.6	0.96	6.12	10.87	4.75
3	5NiO/2CeO_2-SBA-15-CTA	4.7/2.2	13.1/n.a.	619.8	0.88	6.12	11.17	5.05
4	5NiO/5CeO_2-SBA-15-CTA	4.9/5.5	12.7/7.2	574.3	0.78	5.92	10.87	4.95
5	5NiO/5CeO_2-SBA-HCl	5.4/5.5	13.2/7.2	499.3	0.64	5.85	10.42	4.57
6	5NiO/10CeO_2-SBA-15-CTA	5.7/10.1	11.8/7.3	540.2	0.75	5.91	10.81	4.90
7	5NiO/15CeO_2-SBA-15-CTA	5.3/15.4	11.5/7.6	500.9	0.67	5.68	10.74	5.06
8	5NiO/20CeO_2-SBA-15-CTA	5.3/20.1	11.4/8.1	483.7	0.66	5.80	10.69	4.89
9	5NiO/30CeO_2-SBA-15-CTA	5.1/28.1	8.9/8.9	377.4	0.50	5.81	10.40	4.49
10	5NiO/50CeO_2-SBA-15-CTA	4.8/53.7	8.0/9.1	-	-	-	-	-

[a] Determined from XRF measurements.

[b] Calculated by Scherrer's equation from the (200) plane of NiO and (111) plane of CeO_2 in XRD profiles.

[c] a_0 calculated by d_{100}, $a_0 = 2 * d_{100}/\sqrt{3}$.

[d] Pore wall thickness = a_0-D_p.

Fig. 5 displayed the XRD patterns of 5NiO/xCeO_2-SBA-15-CTA catalysts. From the low-angle XRD analysis (Fig. 5A), three typical peaks between 2θ = 0.5-6.0° were found for all the samples, attributing to (100), (110) and (200) planes respectively. Results indicated the presence of 2D ordered hexagonal mesoporous structure (p6mm) even after doping with CeO_2 [30]. The diffraction intensities decreased along with

increasing of CeO_2 content, while the peak position shifted to higher angles. As depicted in Table 1, the calculated unit-cell parameter a_0 decreased from 11.17 nm for 5NiO/2CeO_2-SBA-15-CTA to 10.40 nm for 5NiO/30CeO_2-SBA-15-CTA, which mainly resulted from the local blockage of the pores of SBA-15-CTA, as reflected from the variations of specific surface area [31].

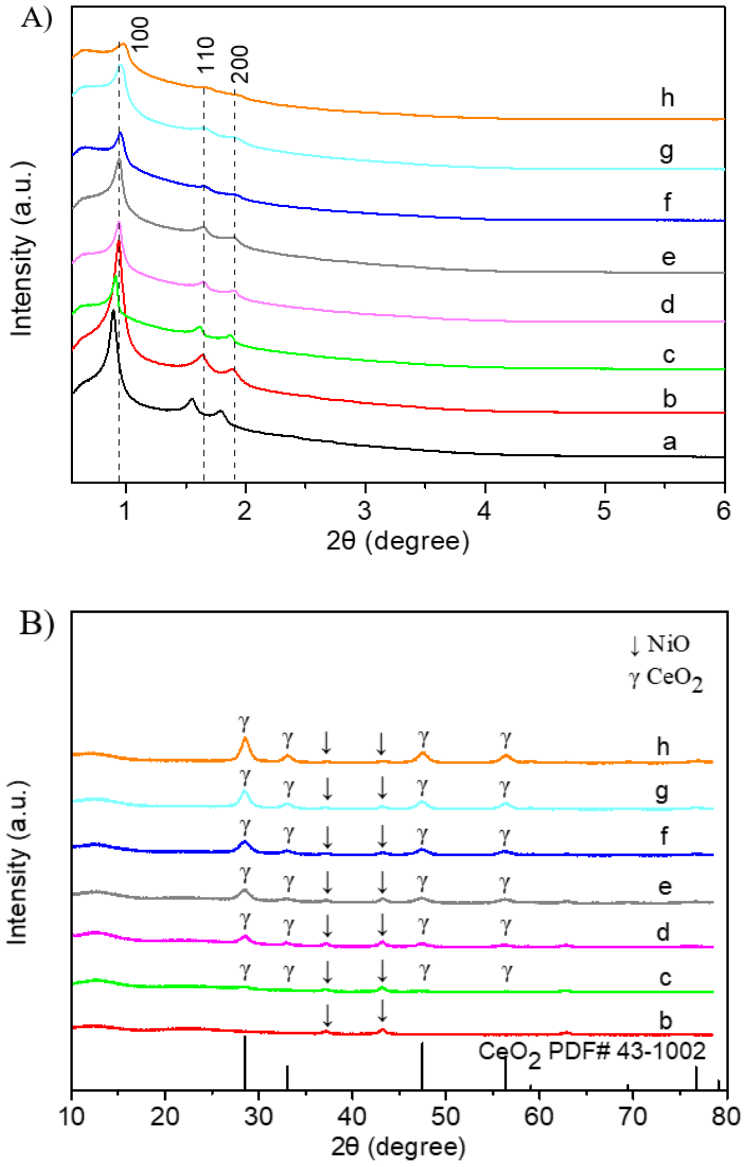

Fig. 5 Low-angle (A) and normal (B) XRD patterns for the 5NiO/SBA-15-CTA and CeO_2 doped 5NiO/SBA-15-CTA catalysts (a) SBA-15-CTA, (b) 5NiO/SBA-15-CTA, (c)

5NiO/2CeO_2-SBA-15-CTA, (d) 5NiO/5CeO_2-SBA-15-CTA, (e) 5NiO/10CeO_2-SBA-15-CTA, (f) 5NiO/15CeO_2-SBA-15-CTA, (g) 5NiO/20CeO_2-SBA-15-CTA, (h) 5NiO/30CeO_2-SBA-15-CTA.

As displayed in the wide-angle XRD patterns (Fig. 5B), it was found that the diffraction intensity of CeO_2 increased with the increasing of ceria loading in 5NiO/xCeO_2-SBA-15-CTA catalysts, while the diffraction intensity for NiO decreased. It was attributed to the improved dispersion of NiO nanoparticles upon the introduction of CeO_2. Results were consistent with what reported in other catalytic systems [22,32]. Moreover, it was observed that the grain size of NiO was slightly decreased with the increasing of CeO_2 content, whereas the crystallite size of CeO_2 nanoparticles was marginally increased as shown in Table 1. According to our previous reports, the wall thickness would increase when Ce species were incorporated in the silica framework to some extent [26]. Herein, the wall thickness (4.90 nm) varied within a reasonable range, revealing that the doped CeO_2 was mainly located on the surface and/or in the channel of the SBA-15-CTA support.

3.2.2 Reduction behaviors

In order to study the reducibility of NiO/SBA-15-CTA doped with different contents of CeO_2, H_2-TPR measurements were performed. As indicated in Fig. 6, for ceria-free Ni/SBA-15-CTA catalyst, an obvious reduction peak with a maximum temperature around 442 ºC was found, owing to the reduction of NiO on SBA-15-CTA carrier. Unlike the reported range of 330-360 ºC for NiO reduction on SBA-15 materials

[16,23], our SBA-15-CTA indicated a stronger interaction between SiO_2 carrier and Ni, leading to a higher reduction temperature at 442 °C. Essentially, after introducing of CeO_2, the first reduction peak became narrower and shifted to the lower temperature. With 2-5 wt.% of CeO_2, the reduction temperatures were significantly dropped to 413 °C. The reduction temperature was further decreased to 337 °C, along with the increasing of CeO_2 content up to 30 wt.%. Results revealed that CeO_2 significantly promoted the dispersion of NiO nanoparticles and decreased their reduction temperature [16,34]. On the other hand, two new peaks at about 465 °C and 750 °C were found for the CeO_2 from 10 wt.% to 30 wt.% doped NiO/SBA-15-CTA catalysts. Practically on 5NiO/15CeO_2-SBA-15-CTA catalyst, the broad H_2 consumption peak centered at ca 464 °C became more visible than those of low content CeO_2 doped samples such as 5NiO/10CeO_2-SBA-15-CTA, which could be regarded as the reduction of Ni^{2+} species with strong interaction with CeO_2 and SBA-15 support [16]. The overlapped reduction phenomena mainly originated from the reduction of Ni-Ce-O species and the Ni-hydrosilicates [13,23]. When the content of CeO_2 was increased to 50 wt.%, the second peak shifted to a lower reduction temperature (403 °C), implying that the reduction was further promoted by CeO_2. For the third reduction peak around 750 °C, which was assigned to the reduction of Ce^{4+} to Ce^{3+} species of dispersed ceria phase [13,35]. It's worth to be mentioned that the specific interaction between the NiO and CeO_2 promoter and support are predominant for NiO/xCeO_2-SBA-15-CTA catalysts at the high CeO_2 contents (≧ 15 wt.%).

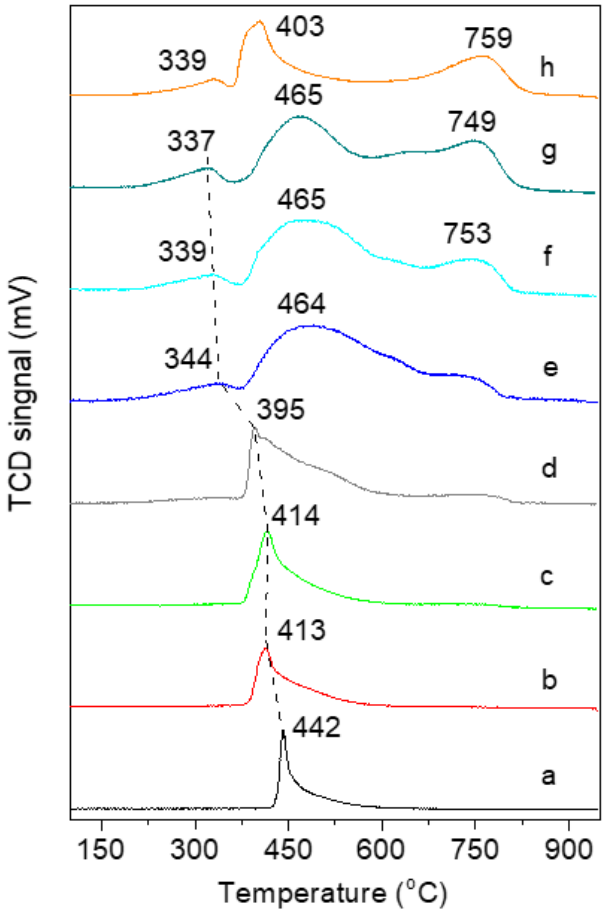

Fig. 6 H_2-TPR profiles of 5NiO/SBA-15-CTA and CeO_2 doped 5NiO/SBA-15-CTA catalysts (a) 5NiO/SBA-15-CTA, (b) 5NiO/2CeO_2-SBA-15-CTA, (c) 5NiO/5CeO_2-SBA-15-CTA, (d) 5NiO/10CeO_2-SBA-15-CTA, (e) 5NiO/15CeO_2-SBA-15-CTA, (f) 5NiO/20CeO_2-SBA-15-CTA, (g) 5NiO/30CeO_2-SBA-15-CTA, (h) 5NiO/50CeO_2-SBA-15-CTA.

3.2.3 XPS measurement

The capability for stabilizing Ni metallic species depends on the strength of metal-support interaction, which can be determined by the concentration of Ce^{3+} to some extend [36-38]. XPS analysis (Fig. 7) was performed on the 5Ni/10CeO_2-SBA-15-CTA and 5Ni/15CeO_2-SBA-15-CTA catalysts. Generally, there exited eight characteristic peaks for Ce 3d XPS spectra, at 882.4, 884.6, 887.4, 899.8, 901.8, 903.9, 906.15, and

917.2 eV, corresponding to u, u′, u″, u‴, v, v′, v″, and v‴ respectively [36,39]. The peaks labeled as u, u″ and u‴ were attributed to the Ce $3d_{5/2}$ spin orbit, while the v, v″, and v‴ peaks were ascribed to the Ce $3d_{3/2}$ component for representing Ce^{4+} state [40]. Another two peaks labeled as u′ (884.6 eV) and v′ (903.9 eV) were related to Ce $3d^9 4f^0 O2p^6$ configuration belonging to the Ce^{3+} state [41,42]. The Ce^{3+} relative concentration percentages of 15.7%, 20.2% and 23.5%, were obtained for the 5Ni/5CeO_2-SBA-15-CTA (patterns are not included in Fig. 7), 5Ni/10CeO_2-SBA-15-CTA and 5Ni/15CeO_2-SBA-15-CTA catalysts, respectively. Substitution of Ce^{4+} by transition elements such as Fe, Co and Ni was proved to increase Ce^{3+} species along with the formation of oxygen vacancies [43,44]. Therefore, it can be speculated that Ni-Ce-O solution was generated especially at the high-loading of ceria, which facilitated the formation of Ce^{3+} species on the surface of mesoporous silica (SBA-15-CTA) carrier.

Table 2 Surface Ce^{3+} relative concentration values and particle sizes of Ni for catalysts

Catalysts	$Ce^{3+}/(Ce^{3+}+Ce^{4+})$ (%)[a]	Fresh samples (nm)[b]	Spent samples (nm)[b]
5NiO/SBA-15-CTA	N.A.	-	-
5NiO/10CeO_2-SBA-15-CTA	20.2	7.6	7.9
5NiO/15CeO_2-SBA-15-CTA	23.5	7.4	7.6

[a] Ce^{3+} content was calculated from the relative area ratio of $Ce^{3+}/(Ce^{3+} + Ce^{4+})$.

[b] Particle size of Ni was obtained the TEM analysis.

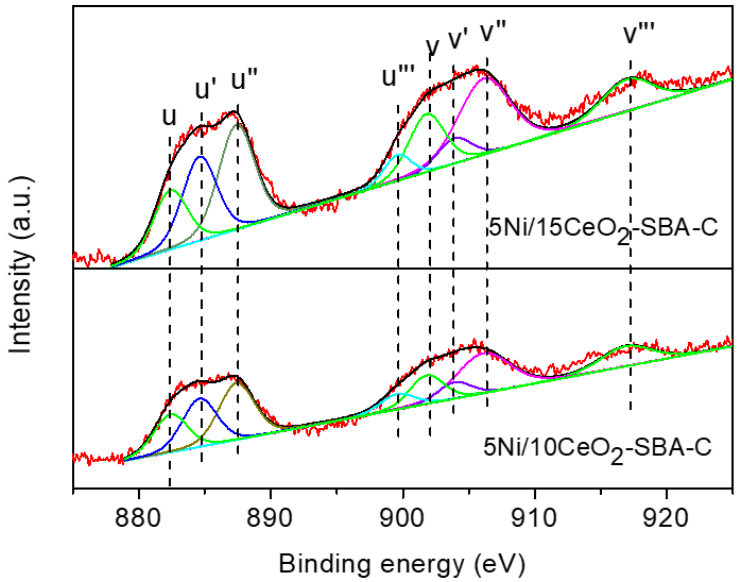

Fig. 7 XPS Ce 3d spectra for reduced catalysts.

3.2.4 Microstructure analysis

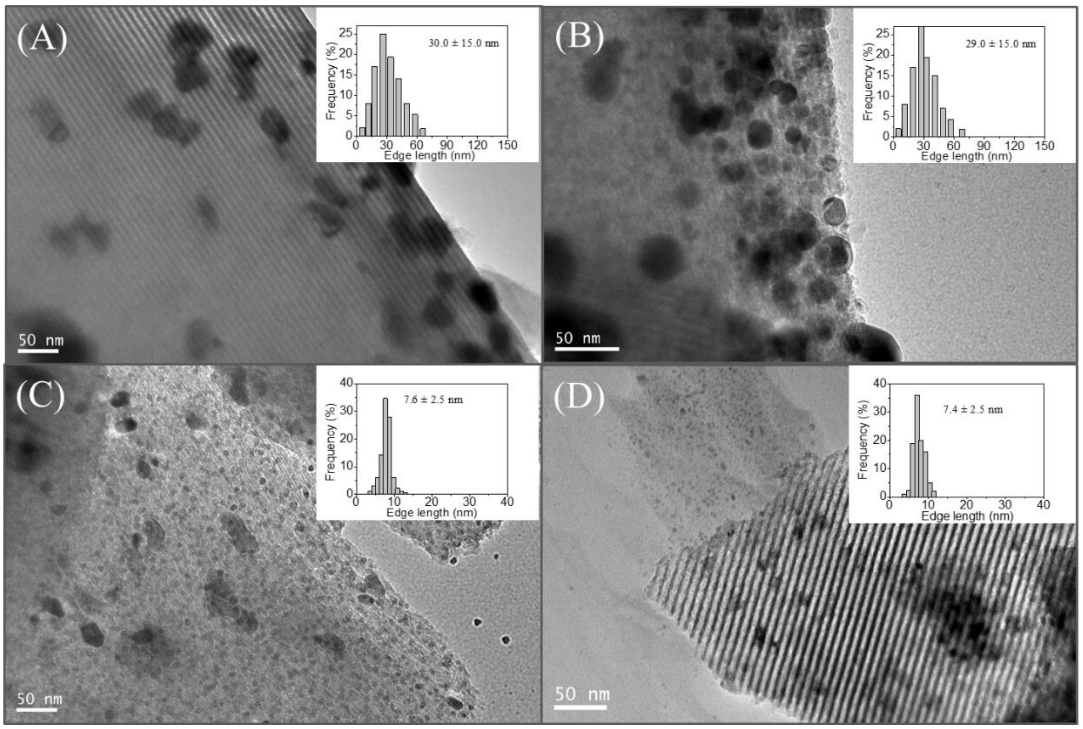

Fig. 8 TEM images of the fresh catalysts (A) 5Ni/SBA-15-CTA, (B) 5Ni/2CeO_2-SBA-15-CTA, (C) 5Ni/10CeO_2-SBA-15-CTA, (D) 5Ni/15CeO_2-SBA-15-CTA.

In order to investigate the relationship between the catalytic activity and microstructure of catalysts, TEM measurements were performed on the representative catalysts, namely 5Ni/SBA-15-CTA, 5Ni/2CeO_2-SBA-15-CTA, 5Ni/10CeO_2-SBA-15-CTA and 5Ni/15CeO_2-SBA-15-CTA catalysts. As showed in Fig. 8, it was found that the 2D mesopores structure of SBA-15-CTA was well retained after the introduction of NiO and CeO_2 on the supports. All the fresh catalysts possessed the typical mesoporous structure. The values of pore size (ca. 6 nm) with a wall thickness of about 5 nm coincided with the above XRD and N_2 physio-sorption data in Table 1. The Ni nanoparticles were not uniformly distributed and agglomerated with particle diameter of 30 nm on the CeO_2 free catalyst (Fig. 8A) and low content of CeO_2 doped 5Ni/2CeO_2-SBA-15-CTA catalysts (Fig. 8B). Improvably, the average Ni sizes can be reduced to about 7.5 nm and evenly distributed on the surface of SBA-15-CTA carrier by increasing the CeO_2 doping contents (10 wt.% and 15 wt.%) (Fig. 8C and 8D), being in good agreement with the data obtained from XRD calculation (Table 1). It provided a direct evidence for the existence of optimum CeO_2 doped content to improve Ni dispersion on the mesoporous silica carrier (SBA-15-CTA).

3.2.5 XAS study of reduced catalysts

XAS is a powerful technique for analyzing the valence state of various elements [45]. As depicted in Fig. 9, compared to the XANES spectra of Ni foil and NiO, there were more Ni being re-oxidized to NiO on the ceria-free 5Ni/SBA-15-CTA catalysts once the pre-reduced catalysts were exposed in the atmosphere condition. On the

contrary, Ni was stable on the CeO_2 doped SBA-15-CTA supports. It can maintain metallic form as indicated in Fig. 9, being consistent with what reported in the literature [23,46]. It was suggested that the addition of CeO_2 played a key role in regulating the valence state of Ni species or stabilizing the metallic state of active Ni species, most probably through the strong interaction between Ni and ceria on mesoporous silica (SBA-15-CTA) matrix [38,47].

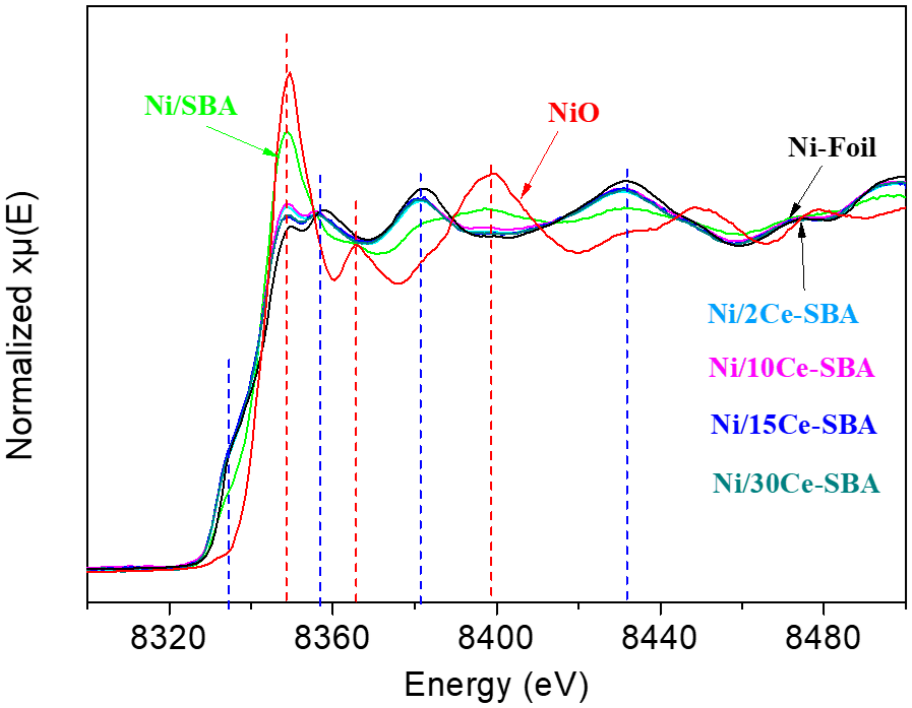

Fig. 9 Ni-K-edge XANES spectra of the reduced catalysts and reference standards (NiO and Ni foil).

3.2.6 Characterization of spent catalysts

Fig. 10 displayed the TEM images recorded on the spent catalysts (5Ni/10CeO_2-SBA-15-CTA after 96 h and 5Ni/15CeO_2-SBA-15-CTA after 170 h reaction). The ordered mesoporous structure of SBA-15-CTA was clearly reserved without significant structural changes on both catalysts. The improved thermal stability of our mesoporous

material (SBA-15-CTA) should be contributed to surface modification of CeO_2 and metallic Ni species. It was reported that the structural collapse of mesoporous silica would be inevitably occurred because of the hydrolysis of surface Si-O-Si bonds during the decarburization reaction [23,48]. Selvaraj's research work revealed that the formation of surface Si-O-Ce bonds hindered the mesoporous structural degradation because of its much higher anti-steam capacity compared to Si-O-Si bonds [49]. As far as the Ni particle size distribution, it was observed that the average Ni particles size was around 7.9 nm for the spent 5Ni/10CeO_2-SBA-15-CTA catalyst (shown in Fig. 10A inset) and 7.6 nm for the spent 5Ni/15CeO_2-SBA-15-CTA catalyst (shown in Fig. 10B inset), which were quite close to those of the fresh catalysts indicated in Fig. 8C and 8D. Results further verified that both CeO_2 doped catalysts presented an excellent resistance to carbon deposition and Ni sintering.

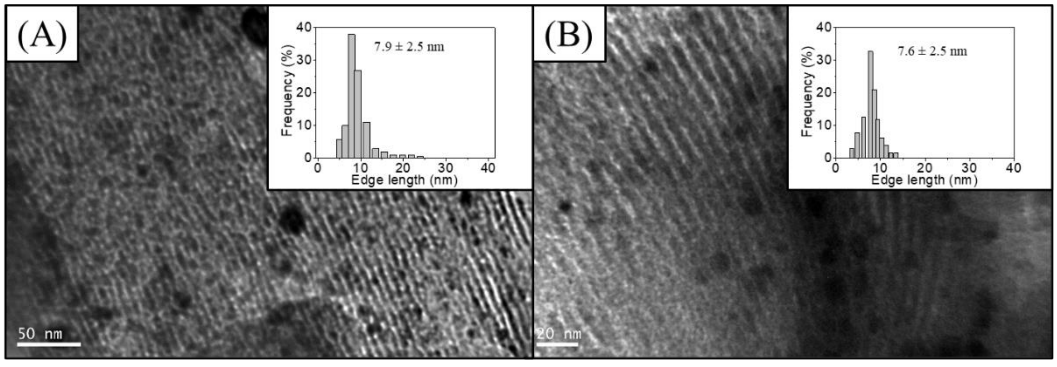

Fig. 10 TEM images of the spent catalysts (A) 5Ni/10CeO_2-SBA-15-CTA used 96 h; (B) 5Ni/15CeO_2-SBA-15-CTA used 170 h.

To summarize, CeO_2 dopants not only improve the metal dispersion, but also enhance the thermal-stability and anti-coke capability of 5Ni/xCeO_2-SBA-15-CTA

catalyst. It was reported that the dispersion or the particle sizes of active Ni species would determine the catalytic activity of Ni-based catalysts for DRM. The well-dispersion Ni particles led to the high catalytic performance [50,51]. The introduction of ceria promoted the dispersion of nickel due to the strong interaction between Ni-Ce mixed oxide. The particle size distribution was strongly influenced by the dopant amount of CeO_2, as presented in Table 1 and Fig 8. In the case of our SBA-15-CTA carrier, the optimal ceria dopant content was likely higher than 10 wt.%, which exhibited a superior catalytic performance than those of the catalysts with low CeO_2 doped content. Further improvements of dopant content (15-30 wt.%) would not significantly improve initial activity. However, the thermal stability and anti-coke capacity were obviously strengthened (Fig. 1D, Fig. 2D and Fig. 10). The weight loss on spent 5Ni/15CeO_2-SBA-15-CTA catalyst was only 13.5% (170 h, Fig. 2D), being much less than that of 5Ni/10CeO_2-SBA-15-CTA spent catalyst (25.4%, 96 h, Fig. 2D). Results reflected that the superior carbon resistance of 5Ni/15CeO_2-SBA-15-CTA catalyst. As a matter of fact, the concentration of Ce^{3+} played an important role in regulating the thermal stability and anti-coke capacity of 5Ni/xCeO_2-SBA-15-CTA catalyst during the DRM reaction. As observed in Table 2, the highest concentration of Ce^{3+} in 5Ni/15CeO_2-SBA-15-CTA catalyst shows the best carbon resistance. As reported by Campbell and his co-worker, the exposed Ce^{3+} ions on CeO_2 were a potentially surface-active sites for catalytic reactions and the generated oxygen vacancies would effectively activate carbon dioxide to mobile oxygen for eliminating deposited coke [52]. The addition of CeO_2 with high content would improve the

probability of substitution of Ce^{4+} by Ni species due to the strong interaction. In particular, the higher the substitution was, the more Ce^{3+} would be generated, leading to a better anti-coke performance.

4. Conclusion

The Ni-CeO_2 catalysts supported over our newly developed SBA-15-CTA carrier with different CeO_2 loadings were successfully prepared and evaluated in dry reforming of methane (DRM) reaction. It was found that SBA-15-CTA can host high CeO_2 dopant amounts up to 30 wt.%, which displayed a high syngas formation rate at a low initiation temperature and anti-coking properties compared with ceria-free Ni/SBA-15-CTA catalyst. The coking resistance capability greatly depended on the hosted ceria dopant amounts. Typically, 5Ni/15CeO_2-SBA-15-CTA catalyst could maintain desirable endurance to thermal stability and anti-coke performance during the long-term DRM reaction for 170 h. Results revealed that the strong interaction between Ni particles and ceria contributed to the well evenly distributed Ni species to give high catalytic performance and suppress the sintering process. Therefore, it was inferred that the high concentration of oxygen vacancy related to Ce^{3+} species would effectively realize the *in situ* removal of coke deposition to improve the anti-coking capability.

Acknowledgment

Authors appreciate Chinese Scholarship Council (CSC) for providing the

scholarship, and Institute of Chemical Engineering and Science (ICES, A*star, Singapore) for the financial support. Thanks for April Wang Zhan, Melissa Prawirasatya, Wen Cong and Wang Luo for their characterization work.

References

[1] N.A.K. Aramouni, J.G. Touma, B.A. Tarboush, J. Zeaiter, M.N. Ahmad, Renew. Sust. Energ. Rev. 82 (2018) 2570–2585.

[2] T. Margossian, K. Larmier, S.M. Kim, F. Krumeich, A. Fedorov, P. Chen, C.R. Müller, C. Copéret, J. Am. Chem. Soc. 139 (2017) 6919-6927.

[3] X.H. Zhang, L. Zhanga, H.G. Peng, X.J.You, C. Peng, X.L. Xu, W.M. Liu, X.Z. Fang, Z. Wang, N. Zhang, X. Wang, Appl. Catal. B Environ. 224 (2018) 488–499.

[4] D. Pakhare, J. Spivey, Chem. Soc. Rev. 43 (2014) 7813-7837.

[5] S. Singh, R. Kumar, H.D. Setiabudi, S. Nanda, D.V.N. Vo, Appl. Catal. A Gen. 559 (2018) 57-74.

[6] Z.Y. Liu, D.C. Grinter, P.G. Lustemberg, T.D Nguyen-Phan, Y.H Zhou, S. Luo, I. Waluyo, E.J. Crumlin, D.J. Stacchiola, J. Zhou, J. Carrasco, H.F. Busnengo, M.V. Ganduglia-Pirovano, S.D. Senanayake, J.A. Rodriguez, Angew, Chem. Int. Ed. 55 (2016) 7455-7459.

[7] K. Mette, S. Kühl, A. Tarasov, M.G. Willinger, J. Kröhnert, S. Wrabetz, A. Trunschke, M. Scherzer, F. Girgsdies, H. Düdder, K. Kähler, K.F. Ortega, M. Muhler, R. Schlögl, M. Behrens, T. Lunkenbein, ACS Catal. 6 (2016) 7238−7248.

[8] F.G. Wang, B.L. Han, L.J. Zhang, L.L. Xu, H. Yu, W.D. Shi, Appl. Catal. B Environ. 235 (2018) 26-35.

[9] S.A. Theofanidis, R. Batchu, V.V. Galvita, H. Poelman, G.B. Marin, Appl. Catal. B Environ. 185 (2016) 42-55.

[10] E. Akbari, S.M. Alavi, M. Rezaei, J. CO_2. Util. 24 (2018) 128-138.

[11] M. Khajenoori, M. Rezaei, F. Meshkani, J. Ind. Eng. Chem. 21 (2015) 717-722.

[12] C. Sun, P. Beaunier, P.D. Costa, Catal. Sci. Technol. 18 (2020): 6330-6341.

[13] Y.X. Yang, C. Ochoa-Hernández, P. Pizarro, V.A.P. Oshea, J.M. Coronado, D.P. Serrano,

Appl. Catal. B Environ. 197 (2016) 206-213.

[14] Q.L. Zhang, T.F. Zhang, Y.Z. Shi, B. Zhao, M.Z. Wang, Q.X. Liu, J. Wang, K.X. Long, Y.K. Duan, P. Ning, J. CO_2 Util. 17 (2017) 10-19.

[15] H.C. Liu, H. Wang, J.H. Shen, Y. Sun, Z.M. Liu, Appl. Catal. A Gen. 337 (2008) 138–147.

[16] D. Li, L. Zeng, X.Y. Li, X. Wang, H.Y. Ma, S. Assabumrungrat, J.L. Gong, Appl. Catal. B Environ. 176 (2015) 532–541.

[17] H. Ay, D. Uner, Appl. Catal. B Environ. 179 (2015) 128-138.

[18] Z.H. Xie, B.H. Yan, S.Kattel, J.H. Lee, S.Y. Yao, Q.Y. Wu, N. Rui, E. Gomez, Z.Y. Liu, W.Q. Xu, L. Zhang, J.G. Chen, Appl. Catal. B Environ. 236 (2018) 280–293.

[19] F.G. Wang, K.H. Han, W.S. Yu, L. Zhao, Y. Wang, X.J. Wang, H. Yu, W.D. Shi, ACS Appl. Mater. Interfaces 12 (2020) 35022-35034.

[20] A. Movasati, S.M. Alavi, G. Mazloom, Int. J. Hydrogen Energy 42 (2017) 16436-16448.

[21] E. Akbari, S.M. Alavi, M. Rezaei, J. CO_2 Util. 24 (2018) 128-138.

[22] S. Damyanova, B. Pawelec, R. Palcheva, Y. Karakirova, M.C. Capel Sanchez, G. Tyuliev, E. Gaigneaux, J.L.G. Fierro, Appl. Catal. B Environ. 225 (2018) 340-353.

[23] S.H. Zhang, S. Muratsugu, N. Ishiguro, M. Tada, ACS Catal. 3 (2013) 1855-1864.

[24] L.M. Li, Z.L. Guo, Y. Liu, W. Chu, J. Solid State Chem. 282 (2020) 121079. https://doi.org/10.1016/j.jssc.2019.121079.

[25] D. Baudouin, U. Rodemerck, F. Krumeich, A.D. Mallmann, K.C. Szeto, H. Ménard, L. Veyre, J-P. Candy, P.B.Webb, C. Thieuleux, C. Copéret, J. Catal. 297 (2013) 27-34.

[26] N. Wang, W. Chu, T. Zhang, X.S. Zhao, Int. J. Hydrogen Energy 37 (2012) 19-30.

[27] F.G. Wang, L.L. Xu, W.D. Shi, J. Zhang, K. Wu, Y. Zhao, H. Li, H.X. Li, G.L. Xu, W. Chen, Nano Res. 10 (2016) 364-380.

[28] H. Wu, J.X. Liu, H.M. Liu, D.H. He, Fuel 235 (2019) 868-877.

[29] K.S.W. Sing, D.H. Everett, R.A.W. Haul, L. Moscou, R.A. Pierotti, J. Rouquerol, T. Siemieniewska, Pure Appl. Chem. 57 (1985) 603-619.

[30] D.Y. Zhao, J.L. Feng, Q.S. He, N. Melosh, G.H. Fredrickson, B.F Chmelka, G.D. Stucky, Science 279 (1998) 548-552.

[31] K. Wang, X.J. Li, S.F. Ji, X.J. Shi, J.J. Tang, Energy Fuels 23 (2009) 25–31.

[32] H.P. Ren, Y.H. Song, W. Wang, J.G. Chen, J. Cheng, J.Q. Jiang, Z.T. Liu, Z.W. Liu, Z.P.

Hao, J. Lu, Chem. Eng. J. 259 (2015) 581-593.

[33] A.Ungureanu, B. Dragoi, A. Chirieac, C. Ciotonea, S. Royer, D. Duprez, A.S. Mamede, E. Dumitriu, ACS Appl. Mater. Interfaces 5 (2013) 3010-3025.

[34] B.M. Al-Swai, N. Osman, M.S. Alnarabiji, A.A. Adesina, B. Abdullah, Ind. Eng. Chem. Res. 58 (2018) 539-552.

[35] N. Wang, K. Shen, L.H. Huang, X.P. Yu, W.Z. Qian, W. Chu, ACS Catal. 3 (2013) 1638-1651.

[36] J. Li, Z.Y. Zhang, Z.M. Tian, X.M. Zhou, Z.P. Zheng, Y.Y. Ma, Y.Q. Qu, J. Mater. Chem. A 39 (2014) 16459-16466.

[37] A. Caballero, J.P. Holgado, V.M. Gonzalez-DelaCruz, S.E. Habas, T. Herranz, M. Salmeron, Chem. Commun. 46 (2010) 1097-1099.

[38] V.M. Gonzalez-DelaCruz, J.P. Holgado, R. Pereñíguez, A. Caballero, J. Catal. 257 (2008) 307-314.

[39] S.H. Zhu, X.Y. Lian, T.T. Fan, Z. Chen, Y.Y. Dong, W.Z. Weng, X.D. Yi, W.P. Fang, Nanoscale 10 (2018) 14031-14038.

[40] K. Kamonsuangkasem, S. Therdthianwong, A. Therdthianwong, N. Thammajak, Appl. Catal. B Environ. 218 (2017) 650-663.

[41] A.P. Ferreira, D. Zanchet, R. Rinaldi, U. Schuchardt, S. Damyanova, J.M.C. Bueno, Appl. Catal. A Gen. 388 (2010) 45-56.

[42] D. Mukherjee, R. Singuru, P. Venkataswamy, D. Damma, B.M. Reddy, ACS Omega 4 (2019) 4770-4778.

[43] S. Tiwari, G. Rathore, N. Patra, A.K. Yadav, D. Bhattacharya, S.N. Jha, C.M. Tseng, S.W. Liu, S. Biring, S. Sen, J. Alloy. Compd. 782 (2019) 689-698.

[44] S. Tiwari, N. Khatun, N. Patra, A.K. Yadav, D. Bhattacharya, S.N. Jha, C.M. Tseng, S.W. Liu, S. Biring, S. Sen, Ceram. Int. 45 (2019) 3823-3832.

[45] Y. Du, Y. Zhu, S. Xi, P. Yang, H O. Moser, M. B. Breese, A. Borgna, J. Synchron. Rad. 22 (2015 839-843.

[46] S. Takenaka, H. Ogihara, I. Yamanaka, K. Otsuka, Appl. Catal. A Gen. 217 (2001) 101-110.

[47] C.E. Daza, J. Gallego, F. Mondragón, S. Moreno, R. Molina, Fuel 89 (2010) 592–603.

[48] K. Cassiers, T. Linssen, M. Mathieu, M. Benjelloun, K. Schrijnemakers, P.V.D. Voort, P. Cool, E.F. Vansant, Chem. Mater**.** 14 (2002) 2317-2324.

[49] M. Selvaraj, D.-W. Park, C.S. Ha, Micropor. Mesopor. Mater. 138 (2011) 94-101.

[50] Q.L. Zhang, K.X. Long, J. Wang, T.F. Zhang, Z.X. Zong, Q. Lin, Int. J. Hydrogen Energy 42 (2017) 14103-14114.

[51] L.B. Raberg, M.B. Jensen, U. Olsbye, C. Daniel, S. Haag, C. Mirodatos, A.O. Sjastad, J. Catal. 249 (2007) 250-260.

[52] C.T. Campbell, C.H.F. Peden, Science 309 (2005) 713-714.